

Wind-Driven Upwelling in the Southern Ocean and the Deglacial Rise in Atmospheric CO₂

R. F. Anderson,^{1,2*} S. Ali,^{1,2} L. I. Bradtmiller,^{1,2†} S. H. H. Nielsen,³ M. Q. Fleisher,¹ B. E. Anderson,¹ L. H. Burckle¹

Wind-driven upwelling in the ocean around Antarctica helps regulate the exchange of carbon dioxide (CO₂) between the deep sea and the atmosphere, as well as the supply of dissolved silicon to the euphotic zone of the Southern Ocean. Diatom productivity south of the Antarctic Polar Front and the subsequent burial of biogenic opal in underlying sediments are limited by this silicon supply. We show that opal burial rates, and thus upwelling, were enhanced during the termination of the last ice age in each sector of the Southern Ocean. In the record with the greatest temporal resolution, we find evidence for two intervals of enhanced upwelling concurrent with the two intervals of rising atmospheric CO₂ during deglaciation. These results directly link increased ventilation of deep water to the deglacial rise in atmospheric CO₂.

Scientists have long sought to unravel the combination of physical and biogeochemical processes responsible for the tight coupling between atmospheric CO₂ concentrations and Earth's climate that has persisted for at least the last 600,000 years (1), with the expectation that knowledge of the processes linking CO₂ and climate in the past will improve projections of future climate change under rising anthropogenic CO₂ levels. It is believed that no single mechanism can account for the full amplitude of past CO₂ variability (2, 3). Although multiple processes operating synergistically may be involved (4, 5), there is general agreement that lower CO₂ levels during glacial periods require increased (relative to interglacials) isolation of deep-water masses from the atmosphere—for example, by increased stratification in the ocean (2, 4–8).

Previous studies [e.g., (2, 9)] have inferred a vital role for the Southern Ocean in regulating glacial-interglacial variability of atmospheric CO₂ because deep-water masses outcrop in the Southern Ocean and exchange gases with the atmosphere. Indirect evidence favoring Southern Ocean control includes the tight coupling between CO₂ and Antarctic temperatures (1, 10–12); the phase relationship between CO₂ and other environmental parameters during deglaciation (5, 13, 14); the widespread distribution of ¹³C-depleted carbon, most likely of deep-sea origin, that invaded the

upper ocean and atmosphere during deglaciation (4, 15, 16); and the precipitous drop during deglaciation in ¹⁴C activity of dissolved inorganic carbon (DIC) in North Pacific intermediate waters, requiring injection of carbon from a reservoir long isolated from the atmosphere, such as the deep sea (17). However, until now there has been no direct evidence for a change in Southern Ocean circulation that could have altered

substantially the partitioning of CO₂ between the atmosphere and the deep sea.

Biogenic opal as an upwelling proxy. Burial of biogenic opal, the microscopic tests of marine diatoms, provides a link to past changes in upwelling and ventilation of deep-water masses in the Southern Ocean. Diatoms live in the euphotic zone where they use dissolved silicic acid (H₄SiO₄) to form opal tests. The zone of maximum production of biogenic silica (opal) occurs just south of the Antarctic Polar Front (APF) (18, 19), corresponding to the region of maximum supply of dissolved nutrients (including Si) to surface waters by upwelling of nutrient-rich deep-water masses (Fig. 1) (20).

Within the zone of maximum opal production, diatom growth throughout spring and summer typically depletes surface waters of dissolved Si supplied during the previous winter (20, 21). Consequently, although the physiological status and growth rate of individual diatom cells may be limited by iron (22), the total amount of biogenic opal produced each year within this region is ultimately limited by the supply of dissolved Si (18–20). Therefore, past changes in the production and burial of opal within this region are tied directly, although not necessarily linearly, to the rate of upwelling.

Deglacial changes in upwelling. Three sediment cores (TN057-13PC, NBP9802-6PC, and E27-23PC; Fig. 2) with relatively high accumulation rates [10 to 20 cm/kyr (10³ years)] were

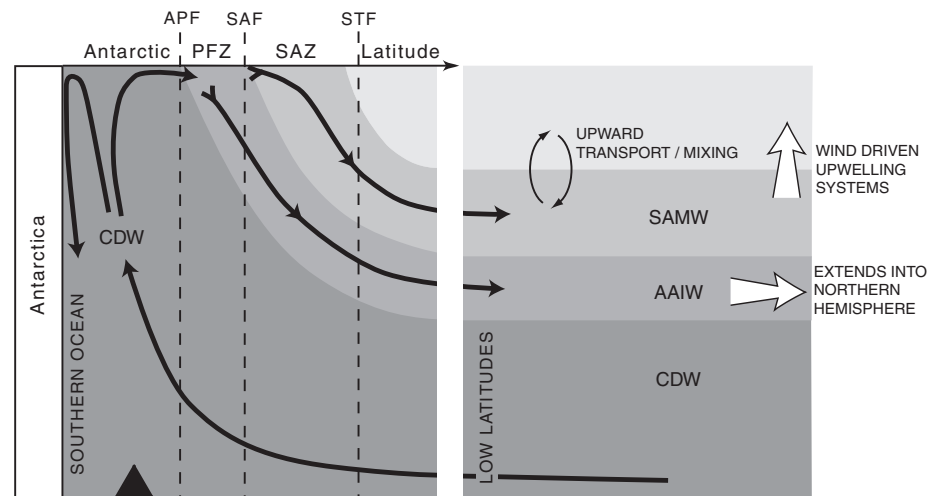


Fig. 1. Water masses entering and leaving the Southern Ocean. Wind-driven upwelling brings Circumpolar Deep Water (CDW) to the surface within the zone south of the Antarctic Polar Front (APF). A portion of the upwelled water moves southward and loses buoyancy, eventually forming Antarctic Bottom Water along the coast of Antarctica. The remainder of the upwelled water moves northward at the surface under the forcing by the prevailing westerlies. Part of the Antarctic surface water mixes with subtropical surface water to form Subantarctic Mode Water (SAMW), a water mass that feeds the thermocline of the Southern Hemisphere (SH) oceans. The densest form of surface water becomes Antarctic Intermediate Water (AAIW), which may be traced northward beyond the equator. Nutrients carried by SAMW are mixed into the surface layer throughout the SH oceans, but especially in upwelling regions such as the eastern equatorial Pacific Ocean (21). The Polar Front Zone (PFZ) and Subantarctic Zone (SAZ) are the regions between the APF and Subantarctic Front (SAF), and between the SAF and Subtropical Front (STF), respectively. Approximate location of cores used in this study from sites just south of the APF is shown by a triangle at the bottom. This figure is modified from figure 4 in (21).

¹Lamont-Doherty Earth Observatory of Columbia University, Post Office Box 1000, Palisades, NY 10964, USA. ²Department of Earth and Environmental Sciences, Columbia University, New York, NY 10027, USA. ³Antarctic Marine Geological Research Facility, Florida State University, Tallahassee, FL 32306, USA.

*To whom correspondence should be addressed. E-mail: boba@ldeo.columbia.edu

†Present address: Department of Marine Chemistry and Geochemistry, Woods Hole Oceanographic Institution, Woods Hole, MA 02543, USA.

selected to provide high-resolution records of opal accumulation during the most recent deglaciation. A fourth core, TN057-14PC, was studied to produce an opal flux record for the last glacial period. The age model for E27-23PC was based initially on biostratigraphy and then was refined with ^{14}C dates of mixed planktonic foraminifera (tables S1 and S2 and fig. S1). We developed an age model for TN057-14PC using biostratigraphy (tables S3 and S4 and fig. S3) that compares well with a published age model (23) based on ^{14}C and ^{18}O (fig. S4). We used published age models for the other cores (24, 25). Opal concentrations were measured spectrophotometrically after alkaline dissolution (26). Sediment burial rates, corrected for sediment focusing, were evaluated with the ^{230}Th -normalization method (27). Uranium and Th isotopes, together with ^{231}Pa , were measured by inductively coupled plasma mass spectrometry (28). A summer (February) sea surface temperature (SST) record for TN057-13PC, constructed by applying the modern analog technique (29, 30) to diatom species assemblages measured at ~ 50 -year resolution, is taken from Nielsen (31).

Each of the three deglacial records (Fig. 3) exhibits a rapid increase in opal flux coinciding with the onset of deglaciation at about 17,000 years ago (ka), followed by a deglacial maximum and declining fluxes into the Holocene (after ~ 10 ka). Most of the opal produced by diatoms in the Southern Ocean is regenerated, either in the water column or during early sediment diagenesis (18, 19), complicating the interpretation of opal fluxes. Therefore, an independent proxy is required to discriminate between changes in opal production (Si supply) versus changes in opal preservation as the ultimate cause of the deglacial maximum in opal burial.

To discriminate between production and preservation of opal, we measured the $^{231}\text{Pa}/^{230}\text{Th}$ ratio of the sediments. Like ^{230}Th , ^{231}Pa is produced uniformly throughout the ocean by radioactive decay of dissolved uranium, and both isotopes are removed from seawater by scavenging onto sinking particles (32). However, ^{231}Pa has a strong affinity for sorption to biogenic opal, and $^{231}\text{Pa}/^{230}\text{Th}$ ratios of particulate material throughout the open ocean are tightly correlated with the opal content of particles (33). Although $^{231}\text{Pa}/^{230}\text{Th}$ ratios of sinking particles and sediments are influenced by particle flux as well as by the opal content of particles, the strong correlation between $^{231}\text{Pa}/^{230}\text{Th}$ ratio and opal flux (25, 34, 35) in many sediment records supports the view that opal flux is the primary variable determining sedimentary $^{231}\text{Pa}/^{230}\text{Th}$ ratios. Furthermore, particulate $^{231}\text{Pa}/^{230}\text{Th}$ ratios are not altered by loss of biogenic phases during early diagenesis of sediments (36), allowing the downcore record of $^{231}\text{Pa}/^{230}\text{Th}$ ratios to be interpreted in terms of past changes in opal flux. Based on the positive correlation between $^{231}\text{Pa}/^{230}\text{Th}$ and opal flux in each of our records (Fig. 3), we conclude that the deglacial maximum in opal flux reflects past

changes in opal production and Si supply rather than variable opal preservation.

Reconstructed opal fluxes indicate maximum rates during deglaciation in each sector of the Southern Ocean (Fig. 3). Shifting circulation patterns and biogeographic provinces to the north or south will not lead to greater biogenic silica production than that occurring today because the core sites are all from the region of maximum dissolved Si supply and opal production in the modern ocean (see above). Therefore, we conclude that the supply of dissolved Si to surface waters south of the APF, which is intimately linked to upwelling of deep-water masses, was at its maximum during deglaciation.

Impact on low-latitude surface waters. Enhanced upwelling in the Southern Ocean during deglaciation would have introduced a chemical signature during the formation of Antarctic Intermediate Water (AAIW) and Subantarctic Mode Water (SAMW), water masses that entrain upwelled deep water during their formation (Fig. 1). Mode waters carry a chemical signature from upwelled deep water (e.g., nutrient concentrations, $\delta^{13}\text{C}$ of DIC) throughout the thermocline of the Southern Hemisphere. This chemical signature is transmitted to surface waters via upward mixing, and it is particularly strong in upwelling regions (21). Spero and Lea (16) invoked this mechanism to explain the deglacial minimum in

$\delta^{13}\text{C}$ of planktonic foraminifera that is observed at many sites throughout the Southern Hemisphere, as well as in a record of the $\delta^{13}\text{C}$ of atmospheric CO_2 derived from the Taylor Dome ice core (15). However, others have been reluctant to use the $\delta^{13}\text{C}$ of planktonic foraminifera as a proxy for entrainment of upwelled deep water because vital effects can overprint the $\delta^{13}\text{C}$ signature from DIC that is incorporated into the shells of foraminifera (4). Therefore, we sought evidence for deep-water injection into the thermocline that would be independent of these effects.

If the deglacial minimum in $\delta^{13}\text{C}$ of planktonic foraminifera were truly a chemical signature of increased upwelling of deep water in the Southern Ocean, then one would expect a contemporary maximum in the supply of dissolved Si and, therefore, in the growth of diatoms in low-latitude regions where water masses originating in the Southern Ocean are known to upwell. This is expected because deep waters are enriched in dissolved Si just as they are in ^{13}C -depleted DIC. To test this prediction, we have determined the accumulation rate of opal at a site in the eastern equatorial Pacific Ocean (EEP), where SAMW upwells today (37) and near the site studied by Spero and Lea (16). There, we find a clear correlation between the deglacial minimum in $\delta^{13}\text{C}$ of *Neogloboquadrina dutertrei* and a corresponding maximum in the

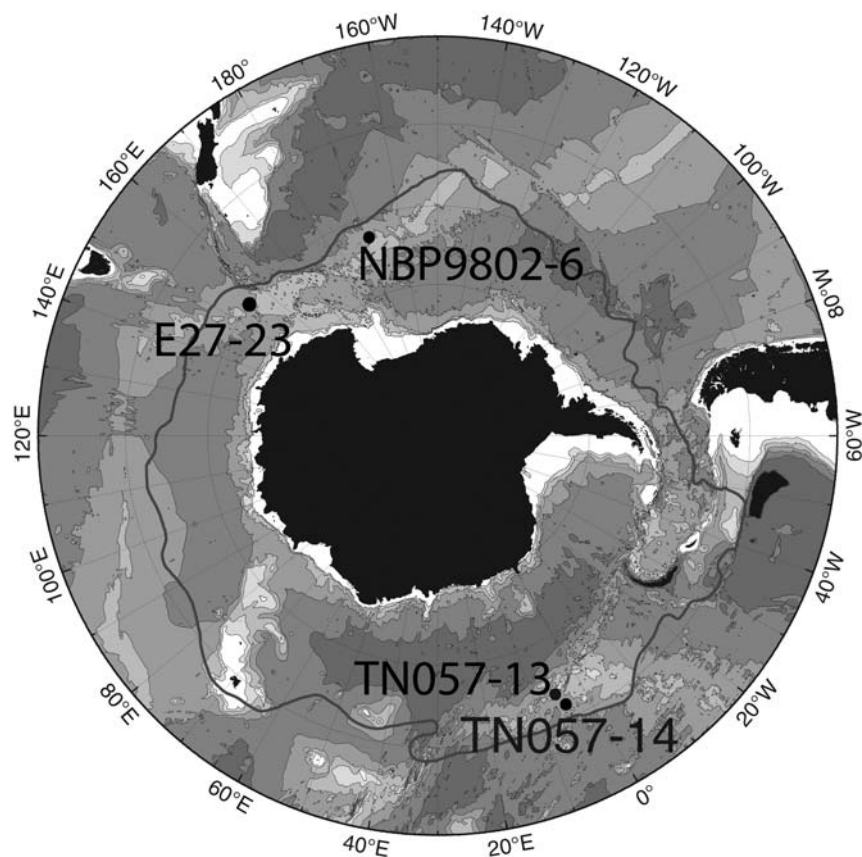


Fig. 2. Locations of cores used in this study. The position of the Antarctic Polar Front (66) is shown as a solid line.

accumulation rate of opal (Fig. 4). *N. dutertrei* is the preferred species to use in such a comparison because it inhabits the deep mixed layer and

upper thermocline, thereby providing the purest record of changes in the chemical composition of waters derived from the Southern Ocean (16).

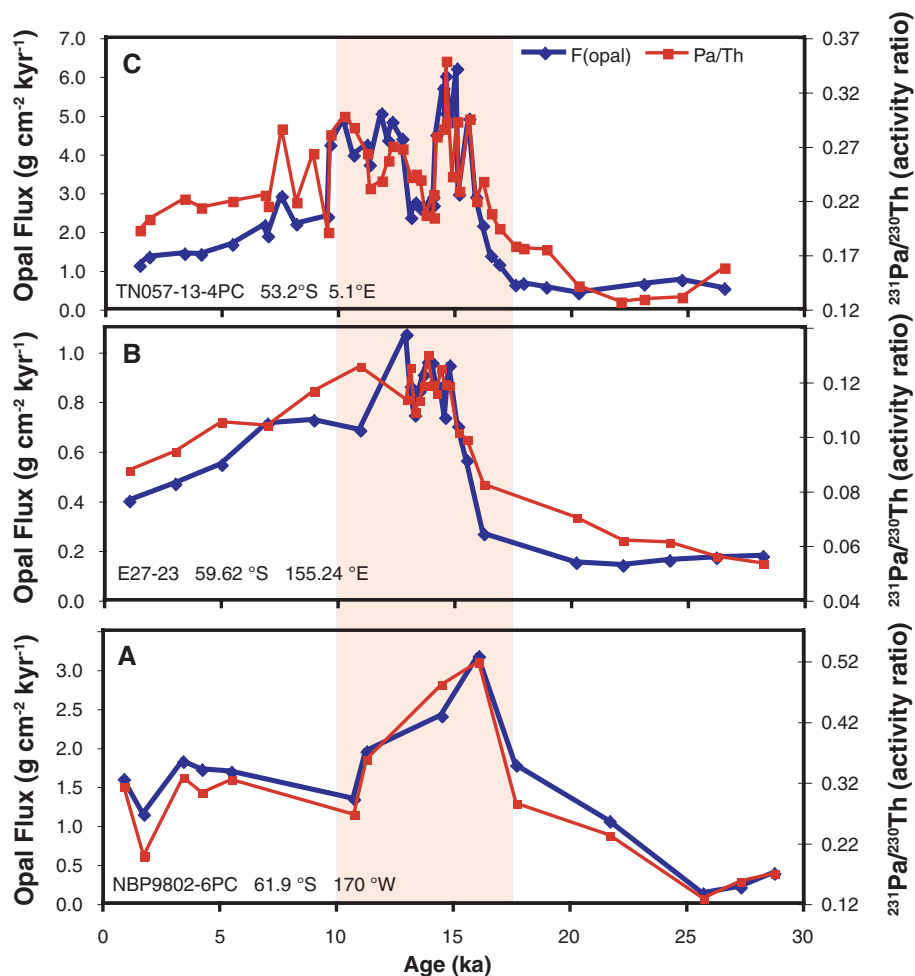


Fig. 3. Opal fluxes, a proxy for upwelling south of the Antarctic Polar Front, from three sites in the Southern Ocean. Increased upwelling during the deglacial period, roughly 17,000 to 10,000 years ago (highlighted in shaded box), is evident in opal fluxes at sites in the Pacific (A), Indian (B), and Atlantic (C) sectors of the Southern Ocean. Initial unsupported $^{231}\text{Pa}/^{230}\text{Th}$ ratios mirror the pattern of opal flux in each core, supporting the view that the opal flux reflects changes in upwelling and opal production rather than changes in opal preservation (see text). Results plotted in (A) are from (25).

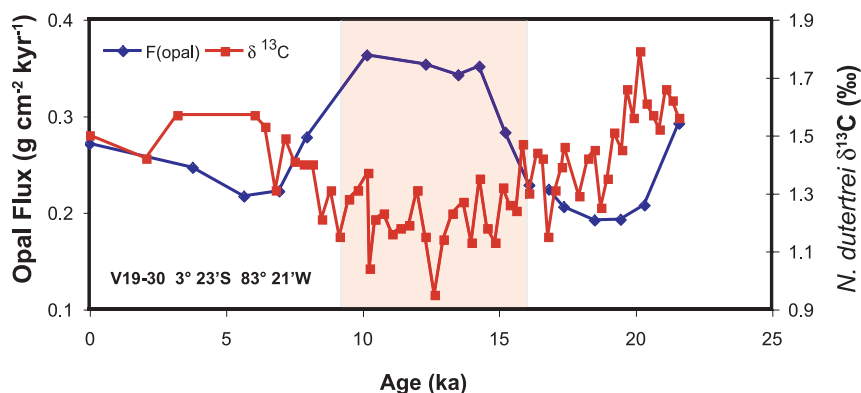


Fig. 4. Two proxy records exhibiting a chemical signature of Southern Ocean water reaching the surface of the eastern equatorial Pacific Ocean. The deglacial minimum in $\delta^{13}\text{C}$ of *N. dutertrei* and the corresponding maximum in opal flux (shaded interval) are both consistent with increased supply of nutrient-rich deep water upwelled in the Southern Ocean during this period (16). Original $\delta^{13}\text{C}$ data from (67); opal data from (34).

Sediment records from other sites in the EEP have also been shown recently to contain a deglacial maximum in opal accumulation (34, 38), indicating that the feature illustrated in Fig. 4 is widespread. Subsequent work has found the deglacial maximum in opal flux to have occurred throughout the equatorial Atlantic Ocean, as well (35). Although other factors (e.g., changes in local upwelling) could have influenced these opal burial records, they are independent of the vital effects thought to overprint the $\delta^{13}\text{C}$ of planktonic foraminifera. Consequently, we interpret the widespread deglacial minimum in $\delta^{13}\text{C}$ of planktonic foraminifera (16), concurrent with the deglacial maximum in opal burial in equatorial upwelling regions, to reflect a period of enhanced entrainment of nutrient-rich deep water during the formation of SAMWs that eventually surface in tropical upwelling regimes.

Link to atmospheric CO_2 . Increased upwelling in the Southern Ocean, inferred from the opal flux records, coincided with the deglacial warming in Antarctica, as well as with the rise in atmospheric CO_2 (Fig. 5, A, C, and D). In TN057-13, the sediment record with the highest temporal resolution, the opal flux declined during the Antarctic Cold Reversal (ACR; ~14.5 to ~12.5 ka), corresponding to a plateau in CO_2 concentration. Although precise age control is lacking for portions of the TN057-13 record, the timing of the ACR is constrained reliably by a radiocarbon date just before its onset (Fig. 5) and by the SST record from this core. Within the resolution of the sample intervals, the decrease in upwelling coincided with the reduction in SST corresponding to the ACR (Fig. 5, B and C). Furthermore, the ACR is also manifest in TN057-13 sediments as a local maximum in the $\delta^{18}\text{O}$ of planktonic foraminifera and by a maximum in the abundance of ice-rafted debris (24), both expected consequences of cooling during the ACR. Increased upwelling resumed following the ACR, coinciding with the second phase of Antarctic warming and rising CO_2 (Fig. 5). The overall timing and character of events recorded in the upwelling proxy record from TN057-13, including the mid-deglacial interruption of upwelling, lead us to conclude that enhanced upwelling of the Southern Ocean was a primary contributor to the deglacial rise in atmospheric CO_2 .

During deglaciation, the $\Delta^{14}\text{C}$ of atmospheric CO_2 dropped by 15 to 20% (Fig. 5E), a much greater change than can be attributed to a contemporary decrease in ^{14}C production, thereby requiring dilution of atmospheric CO_2 with carbon from an older (lower $\Delta^{14}\text{C}$) reservoir (39, 40). Ventilation of the deep ocean around Antarctica, as proposed here, would have supplied the necessary ^{14}C -depleted carbon by exposing the atmosphere to DIC that had been isolated in the deep sea for centuries, if not millennia. Like the rise in atmospheric CO_2 , the deglacial drop in $\Delta^{14}\text{C}$ exhibited a pause coinciding approximately with the reduced upwelling in the Southern Ocean (Fig. 5). Marchitto *et al.*

(17) linked the atmospheric $\Delta^{14}\text{C}$ record to upwelling in the Southern Ocean when interpreting the ^{14}C ages of benthic foraminifera in a core from intermediate depth off the west coast of Mexico. Their results show an injection of ^{14}C -depleted DIC into intermediate waters during deglaciation, occurring in two pulses that coincided with the intervals of rising atmospheric CO_2 . Marchitto *et al.* inferred that the injection of ^{14}C -depleted DIC was a consequence of increased overturning in the Southern Ocean, with the signal being transmitted via AAIW (Fig. 1). Opal fluxes reported here support the interpretation of Marchitto *et al.*, showing periods of increased upwelling coincident with rising atmospheric CO_2 and declining $\Delta^{14}\text{C}$ of CO_2 (Fig. 5).

The deep North Atlantic Ocean. Deglacial changes in the ventilation of the Southern Ocean were associated with deep-water signals at locations as distant as the high-latitude North Atlantic Ocean. For example, coincident with the increased upwelling in the Southern Ocean, deep waters at $\sim 40^\circ\text{N}$ in the Atlantic Ocean are inferred to have borne an Antarctic $\Delta^{14}\text{C}$ signature (41), at a time when sedimentary $^{231}\text{Pa}/^{230}\text{Th}$ ratios are also interpreted to indicate a shutdown of North Atlantic Deep Water formation (42). Furthermore, upper deep waters at $\sim 60^\circ\text{N}$ had a strong Antarctic $\delta^{13}\text{C}$ signature (43) during deglaciation, with a pattern of temporal variability resembling that of the upwelling record from the Southern Ocean (fig. S2).

Northern Hemisphere trigger and atmospheric teleconnection. Two general conditions are believed to have contributed to increased overturning of the Southern Ocean during deglaciation. Watson and Garabato (6) invoked increased heat fluxes into the ocean as a consequence of rising air temperatures. They reasoned that the downward mixing of this surface buoyancy flux would favor increased upwelling. Toggweiler (7) called upon a poleward shift in the mean position of the Southern Hemisphere (SH) Westerlies, with a corresponding increase in northward Ekman transport of surface waters. We propose a combination of these conditions linked to initial forcing within the North Atlantic followed by transmission of the signal to the Southern Ocean via a reorganization of atmospheric circulation.

The onset of rapid warming in Antarctica and the deglacial rise in atmospheric CO_2 concentration coincided with the interval of intense cold in the North Atlantic region surrounding Heinrich Event 1 (HE1) (8, 17, 44). A north-south linkage is further supported by the coincident interruption of Antarctic warming and CO_2 rise during the Bølling-Allerød period of warmth in the north, and the resumption of Antarctic warming and CO_2 rise during the Younger Dryas (YD), another period of intense cold in the Northern Hemisphere (NH). Recent studies have presented evidence for a global reorganization of atmospheric circulation during NH cold events such as HE1 and the YD. Paleo proxy evidence for a southward shift in the Inter-tropical Convergence Zone (ITCZ) during HE1 and/or the YD is found in records from Africa (45, 46), Asia (47), and South America (48–50).

Modeling studies suggest that a southward shift in the ITCZ is a robust feature of atmospheric reorganization, regardless of whether cold NH conditions are induced by imposing sea ice (51) or fresh water (52, 53) on the North Atlantic Ocean.

Less attention has been paid to the westerlies, but lake sediments in Germany record a substantial reorganization of NH westerlies during the YD (54), while rising levels of paleo Lake Lahontan in the western United States during HE1 and the YD are consistent with a southward shift of the NH westerlies during those intervals (55). A rapid warming of SSTs off the coast of Chile at the onset of HE1, and again during the YD, has been attributed to a southward shift of the SH westerlies (44). In support of these findings, five coupled General Circulation Models exhibit a southward displacement of the SH westerlies and an intensification of wind stress at the latitude of the Drake Passage when cold NH conditions are induced by imposing fresh water on the North Atlantic Ocean (56).

An increase in wind stress at the latitude of the Drake Passage is thought to be a key factor regulating upwelling in the Southern Ocean (7). However, enhanced wind stress alone may have been insufficient to increase upwelling. A corresponding increase in baroclinicity of the Antarctic Circumpolar Current would have established a southward eddy transport that largely offset the increase in northward Ekman transport caused by the winds (57). Therefore, it may be necessary to invoke increased buoyancy forcing, possibly

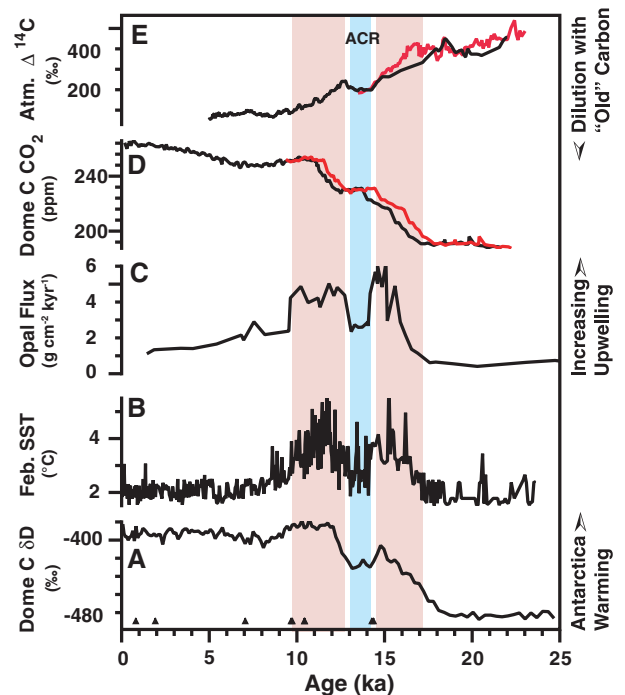
caused by the southward shift of the SH westerlies, via a combination of increased sea-ice divergence, increased precipitation, and direct warming (6), to complement the increased wind stress (7) and fully account for the deglacial increase in upwelling evident in our records (Figs. 3 and 5).

Corresponding events during the last glacial period. Atmospheric CO_2 concentrations rose by 10 to 20 parts per million (ppm) during periods of intense NH cooling throughout the last glacial period (12). Rising CO_2 coincided both with Heinrich Events (between 30 and 60 ka) and with cold intervals before interstadials 19, 20, and 21 (60 to 90 ka). These NH cold intervals corresponded to the warming phase of Antarctic warm events A1 to A7 (58).

Evidence from low latitudes for changes in hydrological conditions at times of NH cooling—for example, in Chinese cave deposits (47) and in the Cariaco Basin (48)—suggests that a global reorganization of atmospheric circulation similar to that proposed for the last deglaciation may have occurred at those times. If true, then shifts in the SH wind system may have been responsible for rising atmospheric CO_2 , and one would expect to find evidence for contemporary increases of upwelling in the Southern Ocean.

To test this possible link between NH cooling and upwelling in the Southern Ocean, we measured the opal accumulation rate in core TN057-14PC, which was recovered from a site $\sim 1^\circ$ north of the location of TN057-13PC (Fig.

Fig. 5. Deglacial records illustrating the coupling between warming in Antarctica, upwelling in the Southern Ocean, and rising atmospheric CO_2 . (A) Deuterium proxy for air temperature over Antarctica from the EPICA Dome C ice core on the EDC1 time scale (68). (B) February SST estimated by applying the modern analog technique (29, 30) to diatom species assemblages extracted from TN057-13PC (31). (C) Opal flux from TN057-13PC (Fig. 3) as a proxy for upwelling in the Southern Ocean. Opal flux and February SST are plotted on the published age model for TN057-13PC (24), based partly on ^{14}C ages from depths in the core indicated by triangles at the bottom of the graph. (D) Atmospheric CO_2 concentrations reconstructed from analysis of the European Project for Ice Coring in Antarctica (EPICA) Dome C (EDC) ice core samples. The black curve is on the EDC1 age model (11, 69). The red curve is the same data placed on the age model of the Greenland Ice Sheet Project 2 (GISP2) ice core (17).



(E) Radiocarbon content of atmospheric CO_2 . The black curve is the INTCAL reconstruction (70). The red curve is the Cariaco Basin record placed on the Hulu Cave age scale (40). Periods of warming in Antarctica are highlighted in red, while the Antarctic Cold Reversal (ACR) is highlighted in blue. The age model for TN057-13 is not constrained well enough during the onset of deglaciation to establish a lead or lag relationship between the onset of increased upwelling and the initial increase in atmospheric CO_2 .

2). Because of changes in the dynamics of the Antarctic Circumpolar Current, conditions that led to the preferential deposition of sediment (sediment focusing) at the site of TN057-13PC during deglaciation were located farther north during the last glacial period. Consequently, it is necessary to combine records from multiple sites when constructing a high-resolution record of opal flux throughout the last glacial cycle. During the interval between 30 and 60 ka, when we have the best constraints on the age model of TN057-14PC (see Supporting Online Material), the opal flux record provides evidence for increased upwelling associated with each period of elevated CO₂ (Fig. 6). Uncertainties in the age model for TN057-14PC do not allow for meaningful assessments of apparent lead-lag relationships between upwelling and CO₂. Rather, the principal conclusion to be drawn from these results is that each interval of elevated CO₂ was accompanied by a period of increased upwelling.

Before 60 ka, constraints for the age model of TN057-14PC are less robust. Nevertheless, the opal flux record indicates increased upwelling associated with Antarctic warm events A5 and A6, and possibly with A7 (Fig. 6). We in-

terpret the general correspondence of elevated CO₂ and increased upwelling with periods of intense NH cooling to indicate a common mechanism operating throughout the last glacial period, as well as during deglaciation. In each case, intense NH cooling induced a reorganization of global atmospheric circulation, leading to a southward shift in the SH westerlies, increased upwelling in the Southern Ocean, and rising atmospheric CO₂ levels. Complementary evidence for a northward shift in the SH westerlies and reduced ventilation of deep water in the Southern Ocean at the onset of glaciation supports this interpretation of a governing role for SH winds (59).

Implications for the future. A southward displacement and intensification of the SH westerlies has been observed in recent decades (60–62). The implications for ocean-atmosphere exchange of CO₂, and for future ocean uptake of anthropogenic CO₂, have been the subject of discussion and debate (63–65). Our evidence for the response of the Southern Ocean to past shifts in the winds may help guide the further development of models used to predict future CO₂ fluxes in this critical region for the exchange of CO₂ between the atmosphere and the deep sea.

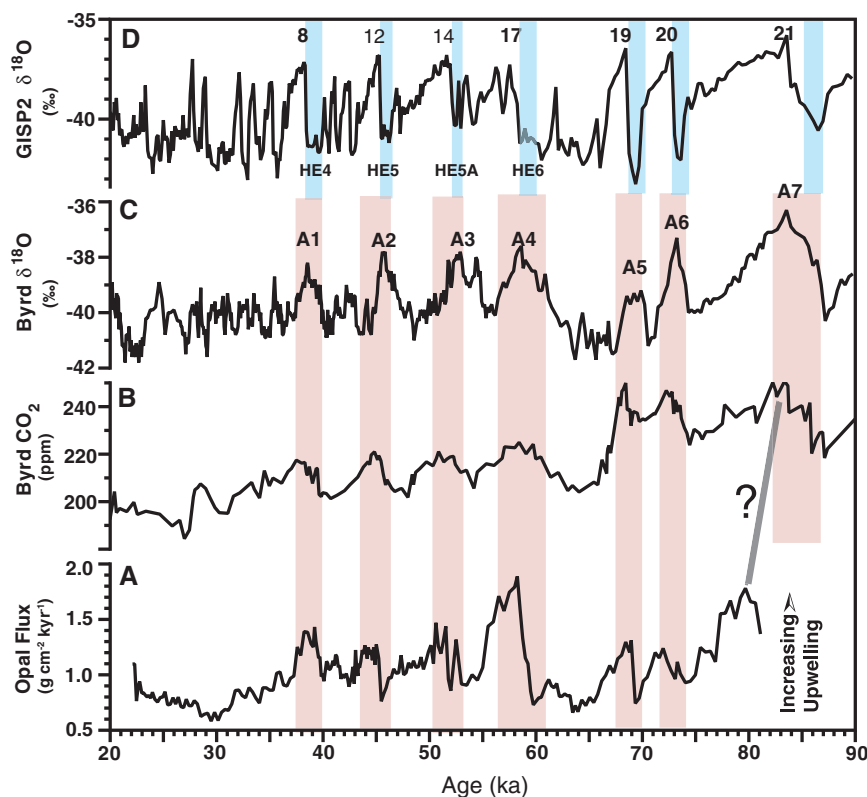


Fig. 6. Records from the last glacial period illustrate the coupling between warming in Antarctica, upwelling in the Southern Ocean, and rising atmospheric CO₂. (A) Opal flux proxy for upwelling in core TN057-14PC (51°59.059'S, 4°30.976'E, 3648 m; Fig. 2) on the GISP2 time scale (figs. S3 and S4). (B) Atmospheric CO₂ from the Byrd ice core on the GISP2 time scale (12). (C) δ¹⁸O of ice in the Byrd ice core on the GISP2 time scale (58). (D) δ¹⁸O of ice in the GISP2 ice core as reproduced in (58). Selected interstadials are labeled in (D). Antarctic warm events (58) are labeled in (C). Blue vertical bars indicate Heinrich Events (71) and cold intervals before interstadials 19 to 21. Red vertical bars indicate periods of relative warmth in Antarctica that include increased upwelling and elevated CO₂. The gray tie-line indicates a possible correlation between upwelling and CO₂ at the bottom of the TN057-14PC record, corresponding to A7, where the age model has an uncertainty of ~5 ka (fig. S4).

References and Notes

- U. Siegenthaler *et al.*, *Science* **310**, 1313 (2005).
- D. M. Sigman, E. A. Boyle, *Nature* **407**, 859 (2000).
- D. Archer, A. Winguth, D. Lea, N. Mahowald, *Rev. Geophys.* **38**, 159 (2000).
- P. Köhler, H. Fischer, G. Munhoven, R. E. Zeebe, *Global Biogeochem. Cycles* **19**, GB4020 10.1029/2004GB002345 (2005).
- S. Peacock, E. Lane, J. M. Restrepo, *Global Biogeochem. Cycles* **20**, GB2010 10.1029/2005GB002448 (2006).
- A. J. Watson, A. C. N. Garabato, *Tellus B Chem. Phys. Meteorol.* **58**, 73 (2006).
- J. R. Toggweiler, J. L. Russell, S. R. Carson, *Paleoceanography* **21**, 10.1029/2005PA001154 (2006).
- D. M. Sigman, A. M. de Boer, G. H. Haug, in *Ocean Circulation: Mechanisms and Impacts*, A. Schmittner, J. C. H. Chiang, S. R. Hemming, Eds. (American Geophysical Union, Washington, DC, 2007), pp. 335–349.
- R. François *et al.*, *Nature* **389**, 929 (1997).
- J. R. Petit *et al.*, *Nature* **399**, 429 (1999).
- E. Monnin *et al.*, *Science* **291**, 112 (2001).
- J. Ahn, E. J. Brook, *Science* **322**, 83 (2008).
- W. S. Broecker, G. M. Henderson, *Paleoceanography* **13**, 352 (1998).
- N. Caillon *et al.*, *Science* **299**, 1728 (2003).
- H. J. Smith, H. Fischer, M. Wahlen, D. Mastroianni, B. Deck, *Nature* **400**, 248 (1999).
- H. J. Spero, D. W. Lea, *Science* **296**, 522 (2002).
- T. M. Marchitto, S. J. Lehman, J. D. Ortiz, J. Fluckiger, A. van Geen, *Science* **316**, 1456 (2007).
- P. Pondaven *et al.*, *Nature* **405**, 168 (2000).
- D. M. Nelson *et al.*, *Deep Sea Res. Part II Top. Stud. Oceanogr.* **49**, 1645 (2002).
- T. Trull, S. R. Rintoul, M. Hadfield, E. R. Abraham, *Deep Sea Res. Part II Top. Stud. Oceanogr.* **48**, 2439 (2001).
- J. L. Sarmiento, N. Gruber, M. A. Brzezinski, J. P. Dunne, *Nature* **427**, 56 (2004).
- P. W. Boyd *et al.*, *Nature* **407**, 695 (2000).
- S. H. H. Nielsen, D. A. Hodell, G. Kamenov, T. Guilderson, M. R. Perfit, *Geochem. Geophys. Geosyst.* **8**, Q12005 (2007).
- A. Shemesh *et al.*, *Paleoceanography* **17**, 1056 10.1029/2000PA000599 (2002).
- Z. Chase, R. F. Anderson, M. Q. Fleisher, P. Kubik, *Deep Sea Res. Part II Top. Stud. Oceanogr.* **50**, 799 (2003).
- R. A. Mortlock, P. N. Froelich, *Deep Sea Res. Part I Oceanogr. Res. Pap.* **36**, 1415 (1989).
- R. Francois, M. Frank, M. M. Rutgers van der Loeff, M. P. Bacon, *Paleoceanography* **19**, PA1018 10.1029/2003PA000939 (2004).
- M. Q. Fleisher, R. F. Anderson, *Deep Sea Res. Part II Top. Stud. Oceanogr.* **50**, 693 (2003).
- X. Crosta, J. J. Pichon, L. H. Burckle, *Paleoceanography* **13**, 284 (1998).
- X. Crosta, A. Sturm, L. Armand, J. J. Pichon, *Mar. Micropaleontol.* **50**, 209 (2004).
- S. H. H. Nielsen, thesis, University of Tromsø (2004).
- R. F. Anderson, M. P. Bacon, P. G. Brewer, *Earth Planet. Sci. Lett.* **62**, 7 (1983).
- Z. Chase, R. F. Anderson, M. Q. Fleisher, P. Kubik, *Earth Planet. Sci. Lett.* **204**, 215 (2002).
- L. I. Bratton, R. F. Anderson, M. Q. Fleisher, L. H. Burckle, *Paleoceanography* **21**, PA4201 10.1029/2006PA001282 (2006).
- L. I. Bratton, R. F. Anderson, M. Q. Fleisher, L. H. Burckle, *Paleoceanography* **22**, PA4216 10.1029/2007PA001443 (2007).
- Z. Chase, R. F. Anderson, M. Q. Fleisher, P. Kubik, *Deep Sea Res. Part II Top. Stud. Oceanogr.* **50**, 739 (2003).
- J. R. Toggweiler, K. Dixon, W. S. Broecker, *J. Geophys. Res. Oceans* **96**, 20467 (1991).
- S. S. Kienast, M. Kienast, S. Jaccard, S. E. Calvert, R. Francois, *Geophys. Res. Lett.* **33**, L15607 10.1029/2006GL026651 (2006).
- K. Hughen *et al.*, *Science* **303**, 202 (2004).
- K. Hughen, J. Southon, S. Lehman, C. Bertrand, J. Turnbull, *Quat. Sci. Rev.* **25**, 3216 (2006).
- L. F. Robinson *et al.*, *Science* **310**, 1469 (2005).
- J. F. McManus, R. Francois, J. M. Gheorghi, L. D. Keigwin, S. Brown-Leger, *Nature* **428**, 834 (2004).

43. R. E. M. Rickaby, H. Elderfield, *Geochem. Geophys. Geosyst.* **6**, Q05001 10.1029/2004GC000858 (2005).
44. F. Lamy *et al.*, *Earth Planet. Sci. Lett.* **259**, 400 (2007).
45. J. E. Tierney, J. M. Russell, *Geophys. Res. Lett.* **34**, L15709 10.1029/2007GL029508 (2007).
46. E. T. Brown, T. C. Johnson, C. A. Scholz, A. S. Cohen, J. W. King, *Geophys. Res. Lett.* **34**, L20702 10.1029/2007GL031240 (2007).
47. Y. J. Wang *et al.*, *Science* **294**, 2345 (2001).
48. L. C. Peterson, G. H. Haug, K. A. Hughen, U. Rohl, *Science* **290**, 1947 (2000).
49. X. Wang *et al.*, *Nature* **432**, 740 (2004).
50. C. Placzek, J. Quade, P. J. Patchett, *Geol. Soc. Am. Bull.* **118**, 515 (2006).
51. J. C. H. Chiang, C. M. Bitz, *Clim. Dyn.* **25**, 477 (2005).
52. K. Dahl, A. Broccoli, R. Stouffer, *Clim. Dyn.* **24**, 325 (2005).
53. R. Zhang, T. L. Delworth, *J. Clim.* **18**, 1853 (2005).
54. A. Brauer, G. H. Haug, P. Dulski, D. M. Sigman, J. F. W. Negendank, *Nat. Geosci.* **1**, 520 (2008).
55. L. Benson, M. Kashgarian, M. Rubin, *Palaeogeogr. Palaeoclimatol. Palaeoecol.* **117**, 1 (1995).
56. A. Timmermann *et al.*, *J. Clim.* **20**, 4899 (2007).
57. R. Hallberg, A. Gnanadesikan, *J. Phys. Oceanogr.* **36**, 2232 (2006).
58. T. Blunier, E. J. Brook, *Science* **291**, 109 (2001).
59. A. Govin *et al.*, *Paleoceanography* **24**, PA1202 10.1029/2008PA001603 (2009).
60. D. W. J. Thompson, S. Solomon, *Science* **296**, 895 (2002).
61. G. J. Marshall, *J. Clim.* **16**, 4134 (2003).
62. G. Chen, I. M. Held, *Geophys. Res. Lett.* **34**, L21805 10.1029/2007GL031200 (2007).
63. C. Le Quééré *et al.*, *Science* **316**, 1735 (2007).
64. K. Zickfeld, J. C. Fyfe, M. Eby, A. J. Weaver, *Science* **319**, 570b (2008).
65. R. M. Law, R. J. Matear, R. J. Francey, *Science* **319**, 570a (2008).
66. A. H. Orsi, T. Whitworth, N. Worth, *Deep-Sea Res.* **42**, 641 (1995).
67. N. J. Shackleton, M. A. Hall, J. Line, C. Shuxi, *Nature* **306**, 319 (1983).
68. EPICA Community Members, *Nature* **429**, 623 (2004).
69. E. Monnin *et al.*, *Earth Planet. Sci. Lett.* **224**, 45 (2004).
70. P. J. Reimer *et al.*, *Radiocarbon* **46**, 1029 (2004).
71. H. Rashid, R. Hesse, D. J. W. Piper, *Earth Planet. Sci. Lett.* **205**, 281 (2003).
72. Work described in this paper was funded by a grants/cooperative agreement from the National Oceanic and Atmospheric Administration, by the National Science Foundation, and by the Norwegian Research Council and the Norwegian Polar Institute as part of VISTA project

6535. The views expressed herein are those of the authors and do not necessarily reflect the views of NOAA or any of its sub-agencies. Comments on earlier drafts of the manuscript by J. R. Toggweiler, L. K. Armand, and M.-E. Carr led to substantial improvements. W. S. Broecker brought to our attention the importance of paleo lake level records. Discussions with P. de Menocal, J. McManus, and D. Martinson helped clarify our thinking about processes discussed in this paper. Comments from two anonymous reviewers improved the manuscript. Samples from TN057 cores were provided by the repository at Lamont-Doherty Earth Observatory; samples from E27-23 were provided by the Antarctic Marine Geology Research Facility at Florida State University.

Supporting Online Material

www.sciencemag.org/cgi/content/full/323/5920/1443/DC1
SOM Text
Figs. S1 to S4
Tables S1 to S4
References

20 October 2008; accepted 9 February 2009
10.1126/science.1167441

The Dynamic Control of Kiss-And-Run and Vesicular Reuse Probed with Single Nanoparticles

Qi Zhang, Yulong Li, Richard W. Tsien*

Vesicular secretion of neurotransmitter is essential for neuronal communication. Kiss-and-run is a mode of membrane fusion and retrieval without the full collapse of the vesicle into the plasma membrane and de novo regeneration. The importance of kiss-and-run during efficient neurotransmission has remained in doubt. We developed an approach for loading individual synaptic vesicles with single quantum dots. Their size and pH-dependent photoluminescence change allowed us to distinguish kiss-and-run from full-collapse fusion and to track single vesicles through multiple rounds of kiss-and-run and reuse, without perturbing vesicle cycling. Kiss-and-run dominated at the beginning of stimulus trains, reflecting the preference of vesicles with high release probability. Its incidence was increased by rapid firing, a response appropriate to shape the kinetics of neurotransmission during a wide range of firing patterns.

As a keystone of neuronal communication, the exocytosis and endocytosis of synaptic vesicles may take different forms (1). In full-collapse fusion (FCF), vesicles flatten completely into the plasma membrane, lose their identity, and must be replaced eventually by newly generated vesicles (2). In contrast, transient fusion and retrieval, often called “kiss-and-run” (K&R), would preserve a limited supply of releasable vesicles for reuse (3). Although nonclassical modes akin to K&R have been demonstrated in non-neuronal cells (4–8) and in a specialized calyceal synapse (9), it remains uncertain whether K&R is appreciable in small nerve terminals typical of the mammalian brain, which rely on only a few dozen releasable vesicles (8, 10). Vesicle recycling in these terminals has been studied by optical reporters

such as styryl dyes or synaptopHluorin (synaptopHluorin fused with pH-sensitive green fluorescent protein) (11–15). However, the limited signal-to-noise (S/N) ratio of such probes has left uncertainty about the functional impact of K&R.

Quantum dots have been widely used for applications requiring high S/N ratios (16–18). Those with peak emission at 605 nm and a diameter of ~15 nm (Qdots hereafter; fig. S1A) provided suitable artificial cargo: small enough to fit into the vesicular lumen (~24 nm), yet large enough to be rejected by putative K&R fusion pores (1 to 5 nm) (9, 19). Furthermore, the pH dependence of Qdot emission (17) would allow reporting of exocytotic events, similar to pHluorin-based indicators (20, 21).

Imaging single Qdot-loaded vesicles. Sparse Qdot loading was accomplished by mildly stimulating neurons. Functional synapses in the Qdot images were identified by subsequent FM4-64 staining (Fig. 1A). At many FM4-64-positive synapses, the Qdot signal was close to background ($P > 0.10$,

t test), indicating no Qdot uptake (Fig. 1A). The remaining synapses (~42%) showed higher intensities distributed in two evenly spaced peaks (Fig. 1A). The interpeak spacing matched the unitary Qdot signal determined by blinking, a spontaneous intermittency of photoluminescence (22) ($P > 0.25$, t test). This calibration (23, 24) confirmed that peak 1 corresponded to uptake of a single Qdot per synapse.

Qdot photoluminescence was pH-dependent: It increased by ~15% when pH was raised from 5.48 (intravesicular) to 7.34 (extracellular) (Fig. 1B). Indeed, photoluminescence of single Qdots in pH 7.34 agarose gel [72.1 ± 2.1 arbitrary units (a.u.), $n = 371$] exceeded that in nerve terminals by ~15% ($P < 0.01$, t test), a difference reversibly nullified by perfusion with pH 5.48 solution (fig. S2C). These data suggested that synapse-loaded Qdots were harbored at pH ~5.5, presumably within synaptic vesicles, as seen directly in electron microscopy images (25).

The pH dependence predicted distinct patterns of Qdot photoluminescence upon K&R and FCF (Fig. 1B): K&R would allow protons but not the Qdot to escape, causing transient deacidification and Qdot brightening. FCF would appear as similar Qdot brightening followed by loss of signal as the Qdot departs.

Qdots unambiguously identify FCF and K&R. Qdot-loaded boutons did exhibit different patterns of photoluminescence upon stimulation (0.1 Hz, 2 min; Fig. 1C): (i) baseline noise, (ii) a transient positive deflection (uptick), (iii) an uptick followed immediately by a negative step (downstep), and (iv) patterns ii and iii in sequence. The uptick level showed as a distinct peak ~15% above baseline, distinct from baseline noise (Fig. 1D). Amplitudes of the upticks with or without downsteps were the same (~9.9 a.u., fig. S3A). Invariably, downsteps followed an uptick, were irreversible (236/236 events, fig. S3B), and were identical in amplitude to that of single Qdots ($P > 0.25$, t test), consistent with the disappearance of Qdots after FCF. With or without downsteps, the great majority of upticks were stimulus-locked

Department of Molecular and Cellular Physiology, Stanford University, Stanford, CA 94305, USA.

*To whom correspondence should be addressed. E-mail: rwttsien@stanford.edu